Visual
Abstract

Experimental and numerical assessment of the location-based impact of grouting defects on the tensile performance of the fully grouted sleeve connection

Kulondwa Kahama Espoir, Xie Fuzhe, Chunhua Lu
School of Civil Engineering and Mechanics, Jiangsu University, Jiangsu China
espoirkulondwa@gmail.com, https://orcid.org/0000-0003-3763-6400
xiefuzhe@ujs.edu.cn, lch79@mail.ujs.edu.cn

Isaac Offei
Department of Civil Engineering, University of Louisville, USA
i0offe01@louisville.edu

ABSTRACT. The presence of grouting defects emanating from construction operations constitutes a major threat to the structural integrity of the grouted sleeve connection of precast concrete members. This work presents a location-based assessment of the impact of grouting defects on the tensile performance of the grouted sleeve connection. Twenty-two specimens with different configurations of defects were subjected to a uniaxial tensile experiment. Corresponding numerical models were proposed, validated and used to conduct a sensitivity analysis of the connection to the defect's location while considering different design confinements of grouting materials. Experimental and numerical studies revealed the following outcome: In consideration of confinement parameters, when the defect of size 3d is located in the mid-span anchorage length, the variation of the sleeve-to-bar diameter (ds/d) from 2.66 (lower design limit) to 3.55 (upper design limit) changed the drop in the ultimate capacity from 19% to 44% below the connection's design requirement. The governing parameters of the grout-bar bond stiffness were the defect's location and degree of confinement. This work proposes a theoretical diagnosis model and a risk assessment catalogue as a promising step toward establishing a computerized diagnosis model of the defective connection to enlighten rational maintenance actions in actual construction.

KEYWORDS. Grout-bar bond; Grouting defects; Grouted sleeve connection; Numerical modelling; Risk assessment.

OPEN ACCESS

INTRODUCTION

A s the Precast Concrete (PC) technology continues to thrive in the construction industry, there is a need to ensure the safe transfer of loads at the connections during the erection of the structure and in its lifetime service. While there are various ways of connecting PC members, the use of grouted sleeve connection is more common in the construction industry worldwide [1-4]. It is used in the horizontal and vertical connection of PC structural members, as shown in

Fig. 1 (b,c) [2, 3]. The mechanical properties of this connection are achieved by injecting non-shrink grouting materials to connect the two reinforcement bars within the sleeve dowel, which provides confinement effects of the grouting materials to enhance the grout-bar bond and the tensile resistance of the configuration [5-8]. Recently, there has been increasing research interest to determine the load-bearing capacity of the grouted sleeve connection, establish its mechanical properties, and understand the grout-bar bond performance of the connection.

(a) specimen detailed sketch

(b) Wall panel with sleeve connection

(c) Column erection with sleeve connection
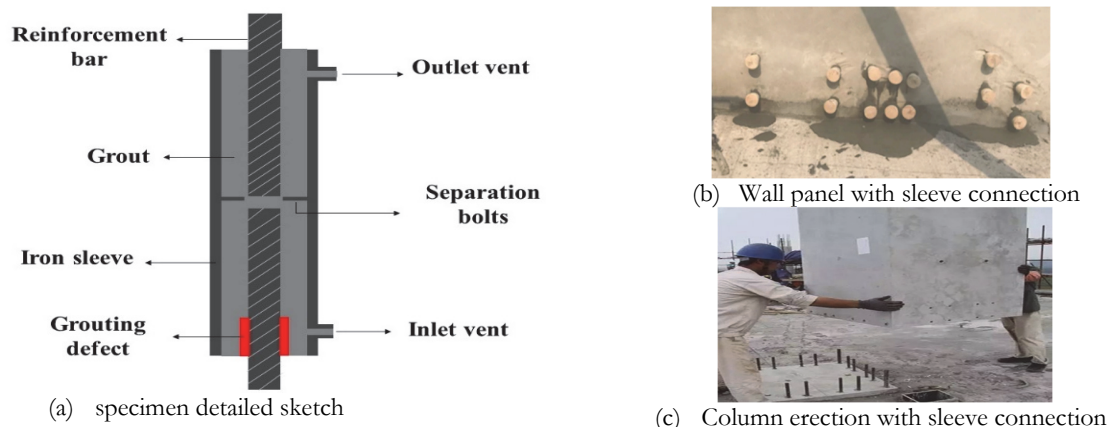
Figure 1: Specimen detailed sketch.

Several experimental works subjected the grouted sleeve connection to uniaxial tensile tests to determine its tensile performance, assess its efficiency to connect reinforcements and achieve at least a similar tensile performance of the continuous reinforcement [9-15]. In common agreement, the findings highlighted the ability of the connection to splice reinforcements to their ultimate tensile capacity and beyond, provided that the connection's components maintain an adequate geometric and mechanical configuration. Key geometric and mechanical parameters influencing the tensile capacity of the connection included the bond strength, the embedded length of the bar and the diameter of the sleeve [3, 16]. The main failure modes encountered were the fracture of the bar and its pullout [12-15]. At the same time, other studies investigated the seismic capacity of the grouted sleeve connection.

In the efforts to waive controversies on the seismic performance of the grouted sleeve connections, multiple studies were conducted to evaluate the seismic strength, crack propagation and energy dissipation in prefabricated concrete members when connected with the grouted sleeve connection [17-26]. The findings of these studies largely contributed to the improvement of the design of the grouted sleeve connection. For instance, in addition to the novel configuration of a seismic-resistant connection proposed by Tong [25, 26], other studies suggested the use of innovative materials such as ultra-high and high-performance (UHPC) grouting materials to improve the connection's seismic Performance [27-29]. Regardless of the significant progress in the design optimization of the grouted sleeve connection, in some cases, the eventual presence of uncontrollable defects within the sleeve remains a major threat to the structural integrity of the connection.

Nowadays, particular research attention is devoted to studying the influence of defects on the performance of the grouted sleeve connection [30-34]. Defects originate from onsite grouting operations through grout leakage in the manipulations of hinges, uplifts of debris by the grouting materials, bubbles, and clogging [33, 35]. Experimental approaches and numerical simulations have been used to investigate the influence of defects on the performance of the grouted sleeve connection [36, 37]. For instance, Xu, et al. [34] considered mixing soil and foam particles in the non-shrink grout injected in half grouted sleeve connection. He realized that 30% occupation of strange particles in the grouting materials weakened the grout-bar bond performance.

On the other hand, Zheng [35] investigated the tensile and cyclic performance of the connection with reduced embedded length defects. He found that the reduction of the embedded length to 5d triggered a pullout failure of the connection, and

its seismic capacity dropped below the design value. Other scholars investigated the influence of defects in the fire performance of the connection [36, 38]. They also discovered that defects would weaken (30% drop in capacity) the post-fire tensile performance of the connection. Nevertheless, the above studies seldom consider the variation of confinement effects in the connection design, which is an influencing factor of the bond stiffness and are inclined to a size-based assessment of the impact of the defects in the half-grouted sleeve, yet the fully grouted sleeve connection can host defects on either or both sides of the reinforcements.

Another attractive research avenue on grouting defects concerns their efficient detection to enhance the structural monitoring and maintenance of the connection. Significant research efforts have been invested in developing accurate detection methods of defects within the connection using nondestructive testing (NDT) [39-44]. Feng et al. [45] proposed a time-reversal ultrasonic waves signal analysis to detect the change in the grout compactness in the sleeve. His method efficiently detected the location of the defects. Zhang et al. [46] used the wavelet packed analysis and dynamic excitation technologies to detect grouting defects in structural members, while Tang et al. [47] developed a deep learning approach to extract defects information from dynamic global data. The major breakthrough in the studies mentioned above is the efficient detection of the defect's location.

In contrast, most published works assess the impact of defects based on their size and cannot, therefore, lead to an accurate defect position-based risk assessment for a rational diagnosis of the defective connection. Moreover, Wang et al. [29] recently demonstrated that the grout-bar bond behavior is highly sensitive to material variation and would likely be differently impacted by defects locations. Therefore, the location-based impact assessment of grouting defects would significantly link the performance assessment of the defective connection to the detected defect to promote an efficient diagnosis and risk assessment of the defective grouted sleeve connection and guide appropriate maintenance action.

This work combines experimental research with numerical modelling to conduct a location-based impact assessment of grouting defects on the tensile performance of the grouted sleeve connection. Three different design confinements of grouting materials are considered to investigate their impact on the performance of the defective connection, and an analysis of the influence of defects locations on the stress distribution among the connection's components was conducted. A theoretical diagnosis model and a risk assessment catalogue are proposed as the first steps toward efficient monitoring and rational risk assessment for systematic and cost-effective maintenance of the defective connection.

MATERIALS PREPARATION AND EXPERIMENT

Material Properties

This study conducted the uniaxial tensile loading test on 22 test specimens embodied with defects in seven different locations. The tensile test of the sleeve revealed that its yield and maximum tensile strengths are 450 MPa and 550 MPa, and total elongation is $\geq$ 7%, in agreement with the design requirements. The reinforcements bars used in this experiment were deformed bars of diameter d=14mm in all the specimens. The tensile properties of the reinforcement were established through a tensile test, as presented in Tab. 1.

Yield strength (MPa)	Ultimate strength (MPa)	Young's Modulus (MPa)	Total Elongation (%)
475.3	623.6	206.5	11.2

Table 1: Properties of the reinforcement bar.

The grouting material was prepared with a water-grout ratio of 13%. The compressive strength test was carried out on 40mm × 40mm × 160mm grout prisms, liquidity and vertical expansion tests were as well conducted to confirm the grouting materials' rheological and mechanical properties, as shown in Fig. 2. The results of these tests are presented in Tab. 2.

Properties	Liquidity	Vertical expansion/(%)	Compressive strength/MPa		
Test time	30 mins	(3h-24h)	(1day)	(3days)	(28days)
Test value	289	0.07	38.8	63.6	97.2

Table 2: Time-dependent mechanical properties of grouting materials

Test specimens and Assemblage

The reinforcement bars were inserted in the sleeve iron with a full anchorage length (l_e) of value 8d, (d, diameter of the bar). Defects were predesigned by wrapping silicon rubber tapes around the reinforcement at different locations, as shown in Fig. 3 (a), while the grout was injected through the inlet vent, and the outflow of grouting material through the inverted L outlet hinge indicates the grout compactness of the connection, as shown in Fig. 3 (b). The strain gauges of the sheet 120-3AA and resistance value of 120 Ω were uniformly installed on the outer surface of the sleeve in both edges and mid-span and on the two reinforcement bars to control the deformation in the connection's components. The overall procedure of the specimen's fabrication can be found in Fig. 3.

(a) Spreading diameter flow

(b) Flow spread expansion

(c) The specimen in the mould

(d) Specimen under compression
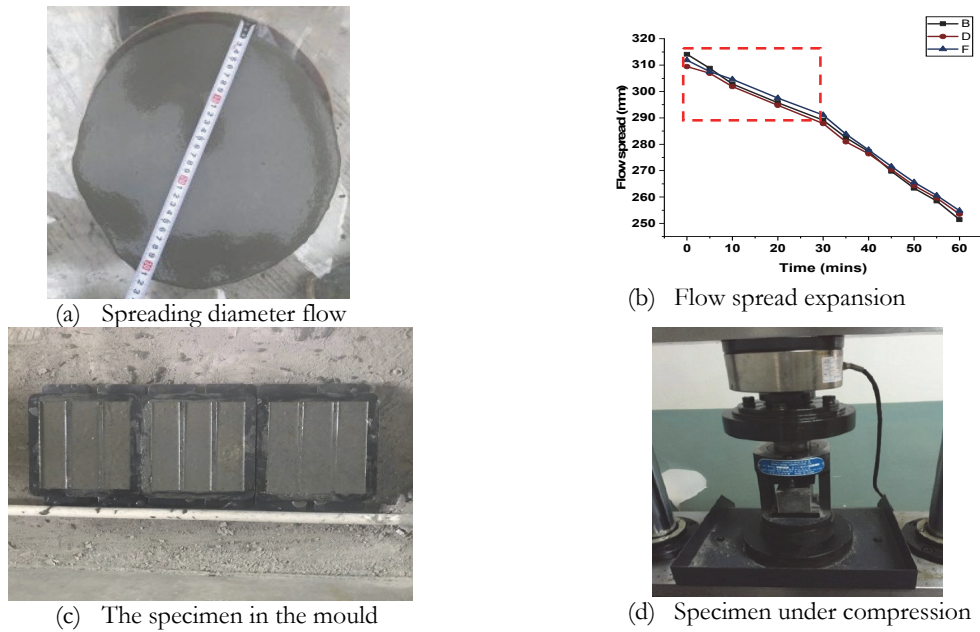
Figure. 2: Tests of grouting materials.

Properties	Liquidity	Vertical expansion/(%)	Compressive strength/Mpa		
Test time	30 mins	(3h-24h)	(1day)	(3days)	(28days)
Test value	289	0.07	38.8	63.6	97.2

Table 2: Time-dependent mechanical properties of grouting materials.

(a) Installation of defects

(b) Grout injection process

(c) Testing strain-gauge

(d) Curing and storage of specimen
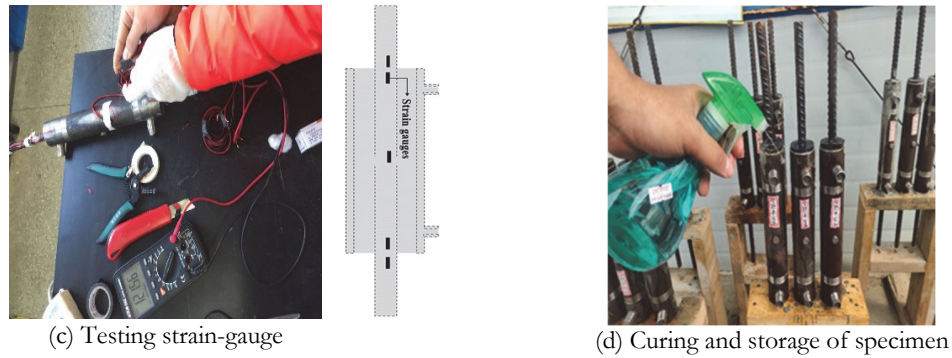
Figure 3: Overall Preparation of the test specimen.

Configuration of specimens

In addition to the non-defective control specimen, 7 different configurations of grouting defects were predesigned based on the common locations of defects in the connection's actual construction process, as shown in Fig. 4. The length of the sleeve was 240 mm, its diameter was 45mm, and the clearance gap between the two reinforcements was 15mm. The silicon rubber defect in this experiment was of 2 mm thickness, wrapped around the reinforcement in 3 major lengths (sizes), including 1d, 2d, and 3d for each configuration tested, respectively. Thus, 22 specimens in total were subjected to uniaxial tensile loading.
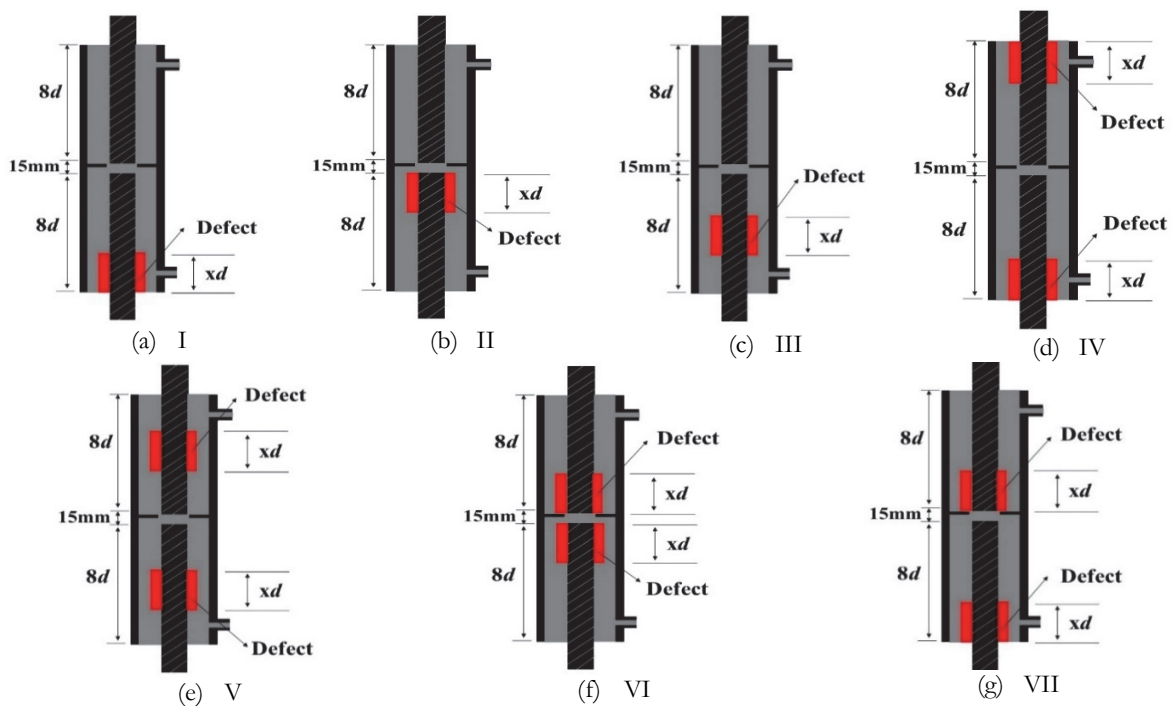
Figure. 4: Configuration of defects in test specimens

The specimens were labelled in order of defect configurations as shown in Fig. 4, the bar's diameter, and the defect's size i.e I-14-1d, as described in Tab. 3.

Loading scheme and test setup

Specimens were subjected to unidirectional static tensile loading based on the Technical Regulations for Mechanical Connection of Steel Bars and Sleeve for Mechanical Connection of Steel Bars, as shown in Fig. 5. The constant loading rate was 28kN/min using a universal testing machine with a maximum capacity of 300kN.

Specimen label	Sleeve material	Rebar diameter (mm)	Defect length (mm)	Defect location detail	Type of defect
F-14	Steel	14	None	None	None
I-14-1d	idem	14	1d	Bottom edge	I
I-14-2d	Idem	14	2d	Idem	I
I-14-3d	Idem	14	3d	Idem	I
II-14-1d	Idem	14	1d	Top of bottom reinforcement	II
II-14-2d	Idem	14	2d	Idem	II
II-14-3d	Idem	14	3d	Idem	II
III-14-1d	Idem	14	1d	Mid - span of lower side	III
III-14-2d	Idem	14	2d	Idem	III
III-14-3d	Idem	14	3d	Idem	III
IV-14-1d	Idem	14	1d	Top & bottom edge	IV
IV-14-2d	Idem	14	2d	Idem	IV
IV-14-3d	Idem	14	3d	Idem	IV
V-14-1d	Idem	14	1d	Mid-span upper & bottom reinforcements	V
V-14-2d	Idem	14	2d	Idem	V
V-14-3d	Idem	14	3d	Idem	V
VI-14-1d	Idem	14	1d	Bottom of upper reinforcement & top of lower reinforcement	VI
VI-14-2d	Idem	14	2d	Idem	VI
VI-14-3d	Idem	14	3d	Idem	VI
VII-14-1d	Idem	14	1d	Bottom of upper reinforcement and lower reinforcement	VII
VII-14-2d	Idem	14	2d	Idem	VII
VII-14-3d	Idem	14	3d	Idem	VII

Table 3: Detailed presentation of all test specimens.
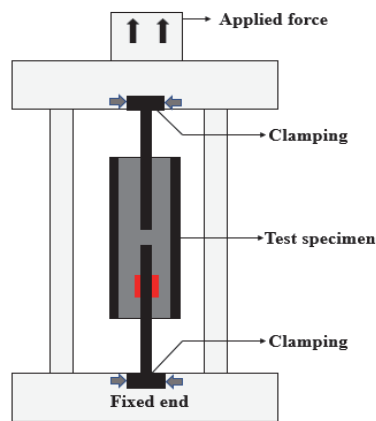
| (a) Sketch of the specimen on the universal testing machine | (b) The specimen on the universal testing machine |
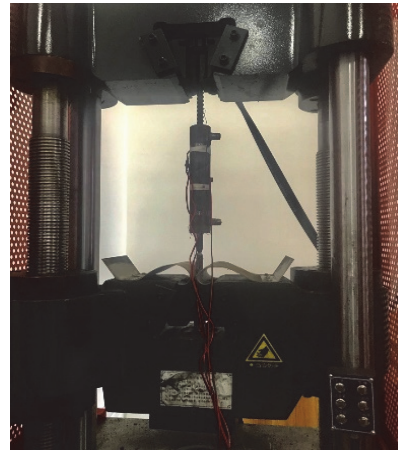
5: Test Specimen subjected to tensile loading

TEST RESULTS AND DISCUSSION

Two main failure modes were observed during the tensile test of specimens: the fracture of the bar and its pullout, as shown in Fig. 7. During the loading process, the yield load and ultimate load as well as their corresponding stresses were measured. Thus, the load-displacement curves are plotted to analyze the performance of each specimen under the tensile loading. Parameters (data) recorded, as shown in Tab. 4, summarize each specimen's response to the uniaxial tensile loading.

Label	Yield force (kN)	Yield Strength (MPa)	Ultimate load (kN)	Ultimate strength (MPa)	Total elongation rate %	Failure mode
F-a	66.26	430.65	95.01	617.51	16.82	Fracture
I -14-1d	67.92	441.44	98.25	638.57	15.86	Fracture
I -14-2d	68.28	378.79	98.23	638.44	16.69	Fracture
I -14-3d	65.51	425.78	97.71	635.06	30.75	Pullout
II -14-1d	66.62	367.99	96.78	616.01	16.42	Fracture
II -14-2d	65.32	424.54	98.36	639.28	18.73	Fracture
II -14-3d	66.25	430.59	97.11	631.16	31.72	Pullout
III-14-1d	65.13	423.31	97.03	630.64	18.52	Fracture
III-14-2d	67.86	441.05	96.97	630.25	26.62	Pullout
III-14-3d	66.39	431.50	79.61	517.42	31.22	Pullout
IV-14-1d	67.48	438.58	98.65	641.17	14.21	Fracture
IV-14-2d	67.04	435.72	98.87	642.60	16.73	Fracture
IV-14-3d	66.88	434.68	95.58	621.21	28.32	Fracture
V-14-1d	66.40	431.56	97.44	633.30	13.23	Fracture

V-14-2d	65.77	427.47	95.67	621.80	24.65	Fracture
V-14-3d	68.67	446.31	84.30	567.40	29.68	Pullout
VI-14-1d	66.59	432.80	98.78	642.01	14.33	Fracture
VI-14-2d	60.21	391.33	98.87	642.60	21.65	Fracture
VI-14-3d	63.12	410.24	96.03	637.40	27.83	Pullout
VII-14-1d	65.82	427.79	98.64	628.10	16.59	Fracture
VII-14-2d	66.42	366.70	96.65	628.10	22.41	Fracture
VII-14-3d	65.29	359.35	96.23	625.44	26.09	Pullout

Table 4: Summary of test results

Position-based impact of grouting defects

Based on the experimental results, defects impacted the tensile performance of the connection differently based on their location and size. The impact of defects based on size has been widely investigated. Thus, in this work, the leading variable in assessing the impact of defects is their location. The performance indices are limited to ultimate tensile load, failure mode, and displacement. The load-displacement curves in Fig. 6 are plotted to supplement the data in Tab. 4 to enlighten the following discussion using a case by case analysis on the impact of defects based on their location.
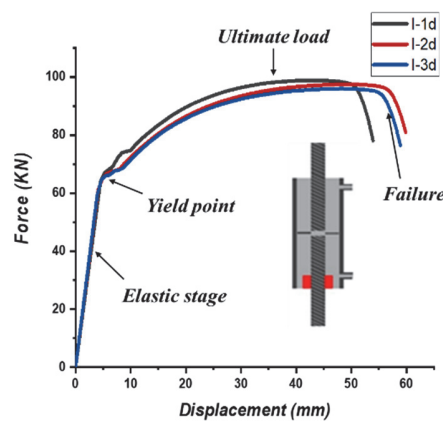
(a)   I specimen L-D curve
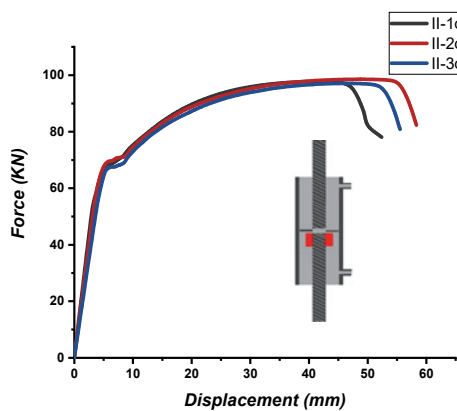
(b)   II specimen L-D curve

(c)   III specimen L-D curve

(d) IV specimen L-D curve

(e) V specimen L-D curve

(f) VI specimen L-D curve
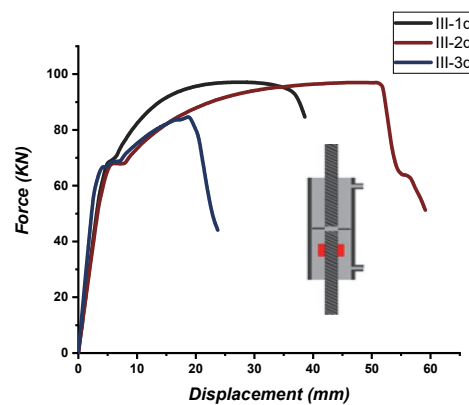
(g) VII specimen L-D curve
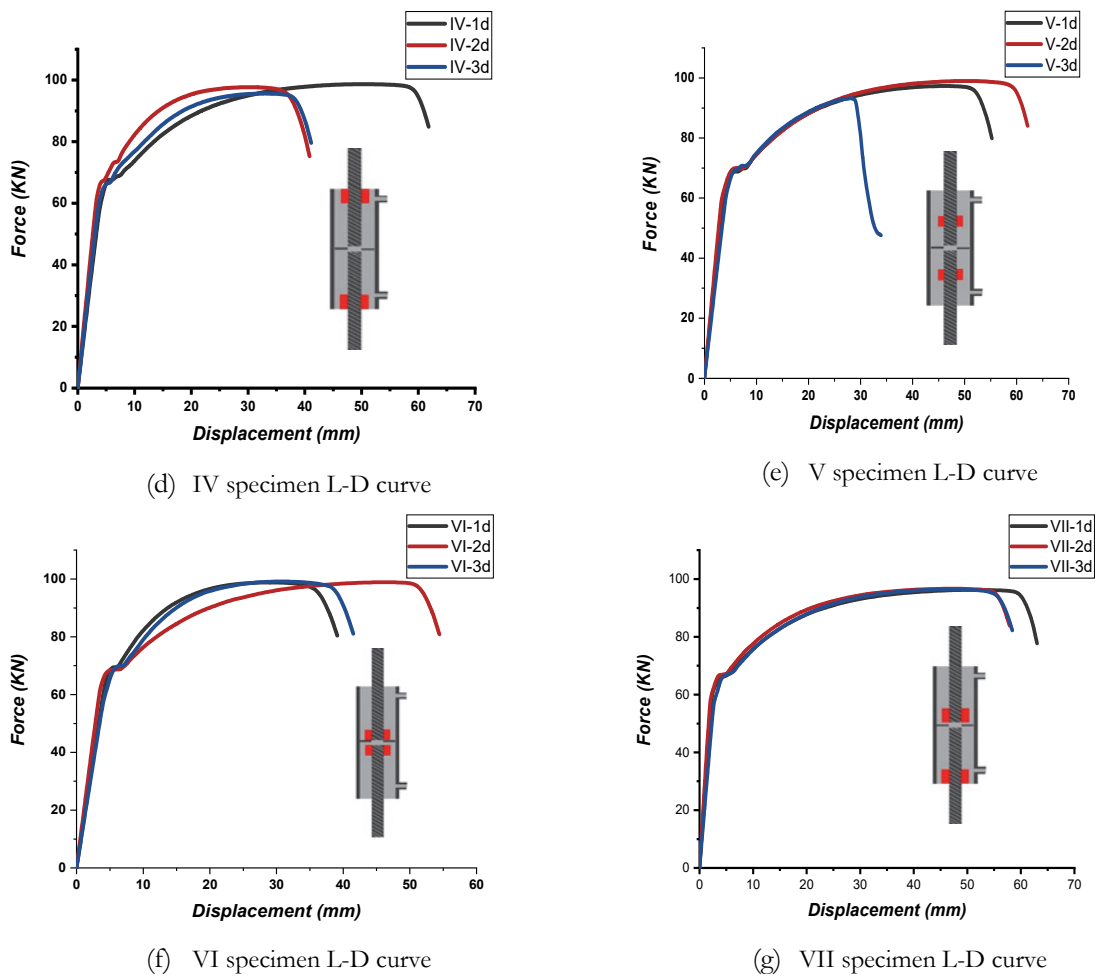
Figure 6: load-displacement curves from experimental research.

In general, as the size of the defect increased, the ultimate capacity of the connection "slightly" decreased while comparing specimens of the same configuration. Regardless of the configuration, the defect of size 1d (14mm) did not significantly impact the connection's performance indices, including the failure modes and load-bearing capacity. Thus an effective anchorage length of 7d met the ultimate design requirements in all the above cases.

The defect of length (2d) 28 mm engendered a pullout failure in only configuration III, while other specimens failed by fracture. This phenomenon indicates that the connection is sensitive to the location of the defect in mid-span anchorage length. Even though the effective anchorage length is 6d, the bond strength is compromised when it is split into two by a 28mm defect, and the connection fails by pullout. The corresponding drop in the ultimate capacity of the connection is about 2-5% when the defect's size is 28mm (2d).

The size (3d) 42 mm defect triggered a significant drop of 20% in the ultimate tensile capacity in configuration III and pullout failures in all other configurations except in configuration IV. It is observed that when the same defect is uniformly replicated on both reinforcements, as in configuration IV, V and VI, the connection has a better performance compared to the configurations with the defect on either the upper or lower reinforcement. This phenomenon is due to the additional stability engendered by the equilibrium of resisting components as the grout-bar bond strength remains almost equal between the two sides. Nevertheless, due to the location of the defect, The equation of the bond strength, in this case, is given as:

$$\mu = \frac{P}{\pi d_b l_b} \qquad (1)$$

P is the force in the bar, πd_b is the nominal perimeter of the bar and l_b is the effective uninterupted anchorage length of the bar. The extent to which defects compromise the bond strength determines the failure mode, as shown in Fig. 7.

| (a) Fracture of the bar failure | (b) Pullout failure |
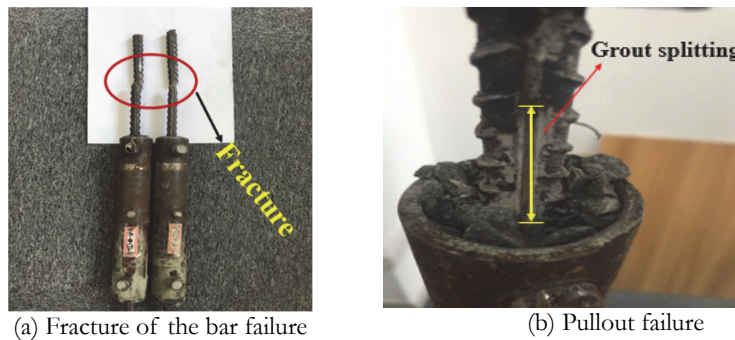
Figure 7: Failure modes during the experiment

In summary, the defect's location can engender a change in the failure mode of the connection and a drop between 0% - 20% in the tensile capacity of the connection, as detailed in Tab. 5.

Configuration / Defect's location	Impact on the tensile capacity		Impact on the failure mode	
	Defect size: 2d	Defect size: 3d	Defect size: 2d	Defect size: 3d
I	0% - 5%	0% - 5%	Fracture	Pullout
II	0% - 5%	0% - 5%	Fracture	Pullout
III	0% - 5%	20%	Pullout	Pullout
IV	0% - 5%	0% - 5%	Fracture	Fracture
V	0% - 5%	8.5 %	Fracture	Pullout
VI	0% - 5%	0% - 5%	Fracture	Pullout
VII	0% - 5%	0% - 5%	Fracture	Pullout

Table 5: Summary of defect's impact based on location.

Based on the above findings, the impact of the defect based on their location can be classified into three major zones of impact, as described in Fig. 8.

| (a) Minor impact | (b) Mild impact | (c) High impact |
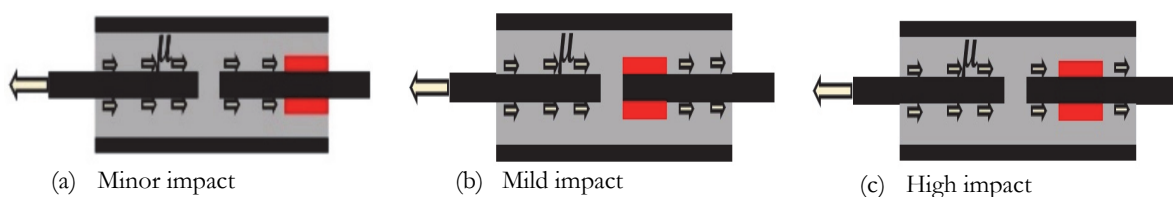
Figure 8: Impact of the defect based on its location in the grouted sleeve connection

PROPOSED FINITE ELEMENT MODEL AND VALIDATION

The model proposed in this work was established and simulated in Abaqus computer-aided engineering (CAE) commercial software in similar experimental boundary and loading conditions.

Materials model

The sleeve was modelled as a hollow cylinder of thickness 6 mm using a bilinear model without considering the materials' hardening strain. The material's properties are shown in Tab. 6.

Mass Density (kg/m³)	Young's Modulus (MPa)	Poisson's ratio	Ultimate strength (MPa)
7300	203000	0.3	550

Table 6**:** Material Properties of the Sleeve.

The reinforcement was modelled using a constitutive model, as shown in Fig. 9 (a), following the conversion of engineering strains from the experiment to true strains using the equations below:

$$\varepsilon_t = l_n \left(1 + \varepsilon_{eng}\right) \tag{2}$$

$$\sigma_t = \sigma_{eng} e^{\varepsilon_t} \tag{3}$$

The corresponding properties are shown in Tab. 7.

Yield strength (MPa)	Ultimate strength (MPa)	Ultimate strain (%)	Young's Modulus (MPa)	Poisson's ratio
7300	203000	0.3	550	0.3

Table 7: Reinforcement bar parameters.

The modelling of grouting materials opted for the Concrete Damaged Plasticity (CDP) model with tensile stiffening in the post-failure modelling of the grouting materials, as shown in Fig. 9, and modified for concrete under confinement based on Lubliner's model [48].

The derivation of the CDP parameters involves a tedious mathematical process with assumptions in the plastic behaviour of concrete. The CDP parameters in this work are based on empirical, experimental studies and are shown in Tab. 8.

The study conducted by Malm [49] on a reinforced concrete beam confirmed that the changes in the dilatation angle between 20^0 and 40^0 do not have a significant impact. Further experimental studies conducted on the same aspect best agreed on the values of the dilatation angle between 30^0 and 40^0 [50, 51]. Szczecina, however, in his computation of selected CDP parameters, confirmed that a dilatation angle approximating 40^0 is more appropriate to simulate concrete under tensile loading [52]. In this work, the best prediction of the concrete performance was achieved at the dilatation 38^0.

The flow potential eccentricity is a small positive number that defines the rate at which the hyperbolic flow potential approaches its asymptote [53]. Its approximative value is 0.1 [54].

The ratio of the biaxial compressive yield to the uniaxial compressive yield (f_{bo} / f_{co}) was assumed to be 1.16 based on Ma's recommendation [55].

The ratio K of the second stress invariant on the tensile meridian was kept at 2/3 based on Ren's derivation [56].

The viscosity parameter is a very low value selected in light of the time increment in Abaqus. This value is significant in static computational analysis and is associated with the convergence of the solution of models with nonlinear materials. Even though the computation in this research followed a quasi-static analysis in the explicit solver where the viscosity parameter has nearly no effect, its value was set at 0.0001 based on Raza's recommendation to keep the value < 0.001 [38].

Mass density (kg/m³)	Elastic modulus MPa	Poisson's ratio	Dilatation angle	Eccentricity	f_{bo} / f_{co}	K	Viscosity parameter
2500	38000	0.2	38	0.1	1.16	0.6667	0.0001

Table 8: Concrete damage Plasticity parameters

| (a) Bar's constitutive model | (b) The behaviour of concrete in compression | (c) The behaviour of concrete in tension |
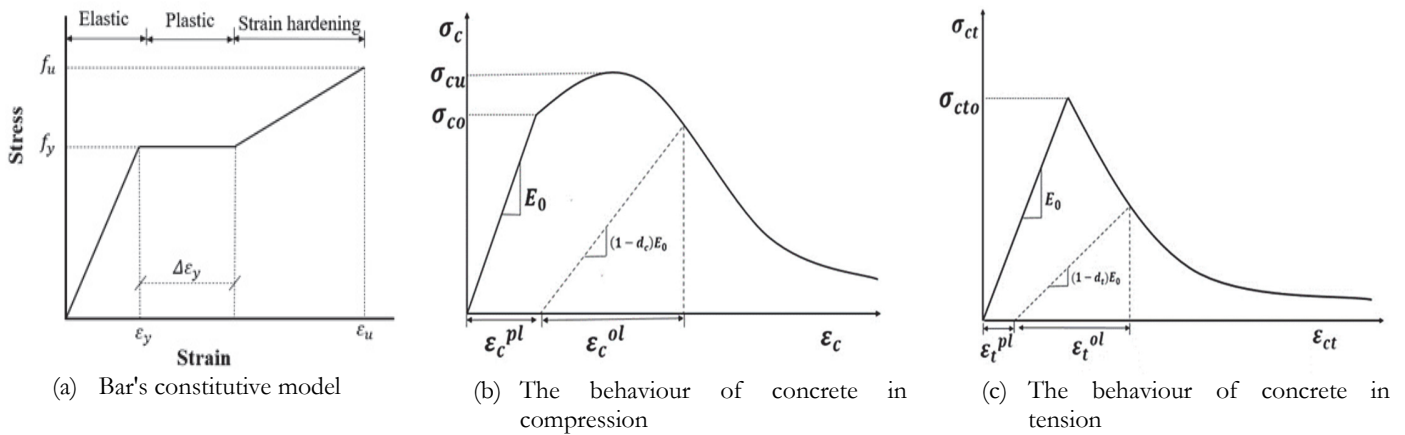
Figure 9: Behavior of modelled materials

Interaction and model computation

The modelling of the grout-bar bond was achieved by a cohesive interfacial model based on the traction separation law and damage initiation criterion. Penalty friction (slipping) was applied to model the second contact the interface after the damage (yielding) of the bond. The mechanical interlocks engendered by ribbed bars in the actual grout-bar bond are accounted for by the interpenetration nodes in a cohesive interaction of the bonding interface in Abaqus. Defects are set as zones of no contact between the reinforcement bar and the grouting materials. The bond-slip behaviour is summarized in Fig. 10.

| (a) Local bond-slip model | (b) Modelling of the bond-slip |

(i) traction separation behaviour   (ii) Friction behaviour
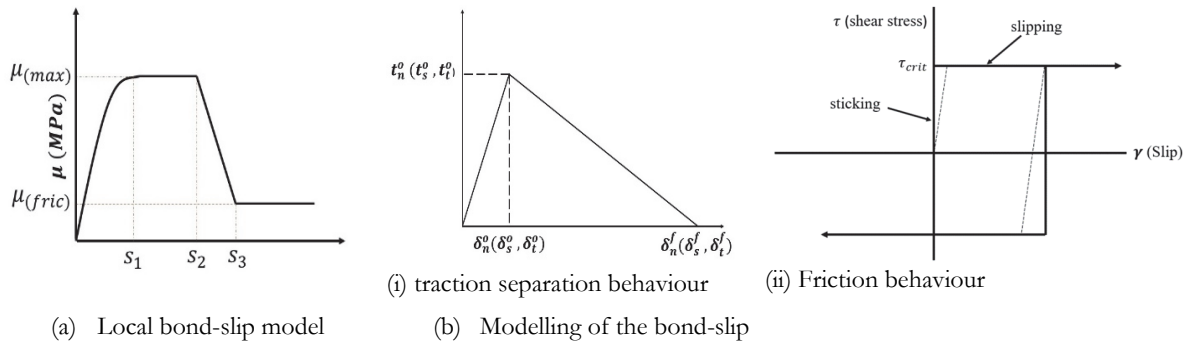
Figure 10: Bond slip behaviour

The damage initiation criterion corresponds to the yielding value of the grout-bar design bond, usually between 15 MPa to 25 MPa. The traction separation law considered traction stress vectors (t), the stiffness coefficient (K), and the corresponding separation stress (δ). The traction stress vector in the normal direction and the two directions of shear is defined by the expression below :

$$t = \begin{Bmatrix} t_n \\ t_s \\ t_t \end{Bmatrix} = \begin{bmatrix} K_{nn} & K_{ns} & K_{nt} \\ K_{ns} & K_{ss} & K_{st} \\ K_{nt} & K_{st} & K_{tt} \end{bmatrix} \begin{Bmatrix} \delta_n \\ \delta_s \\ \delta_t \end{Bmatrix} = K\delta \tag{3}$$

The grout-sleeve interaction is considered in perfect bonding as the interface experiences minimal stress and is in most cases stable under the connection's tensile experiment. The computation of the numerical models was achieved through a quasi-static analysis with boundary conditions and loading schemes reflecting the tensile experiment on the specimens in this work. The displacement load was applied on the upper reinforcement while the lower reinforcement was fixed similarly to the experiment. The meshing of the finite element models adopted the solid linear 3D (C3D8R) element. The mesh size was 2 mm for the grouting materials and the sleeve and 3mm for the reinforcement, and the surfaces of the circular elements included a curvature control, as shown in Fig. 11.

(a) The meshing of the model and loading sketch   (b) Enlarged view of the meshed parts
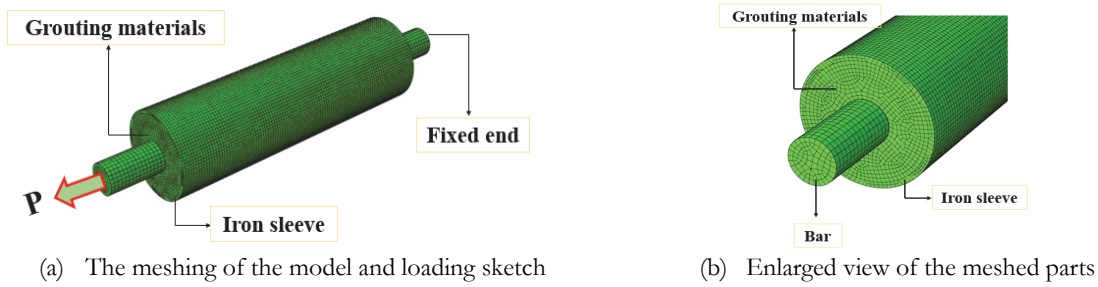
Figure 11: Mesh of the specimen

Models Validation

The validation of the proposed models was achieved by comparing finite element analysis (FEA) load-displacement plots with the experimental plots to assess the reliability of the model's replication in related studies. Failure modes are as well compared to assess the accuracy of the proposed models to simulate the bond behaviour and predict the failure mode of the connection.

Load displacement curves comparison

The validation of the numerical models was conducted by comparing load-displacement curves of simulated specimens with the plots of their corresponding experimental specimens. The configurations II, II and IV were selected for validation when the defect's size is 2d and 3d to test the model's sensitivity to the defects' location, as shown in Fig. 12.

(a) Specimen III-2d L-D comparison

(b) Specimen III-3d L-D comparison

(c) Specimen II-2d L-D comparison

(d) Specimen II-3d L-D comparison

(e) Specimen IV-2d L-D comparison   (f) Specimen II-3d L-D comparison
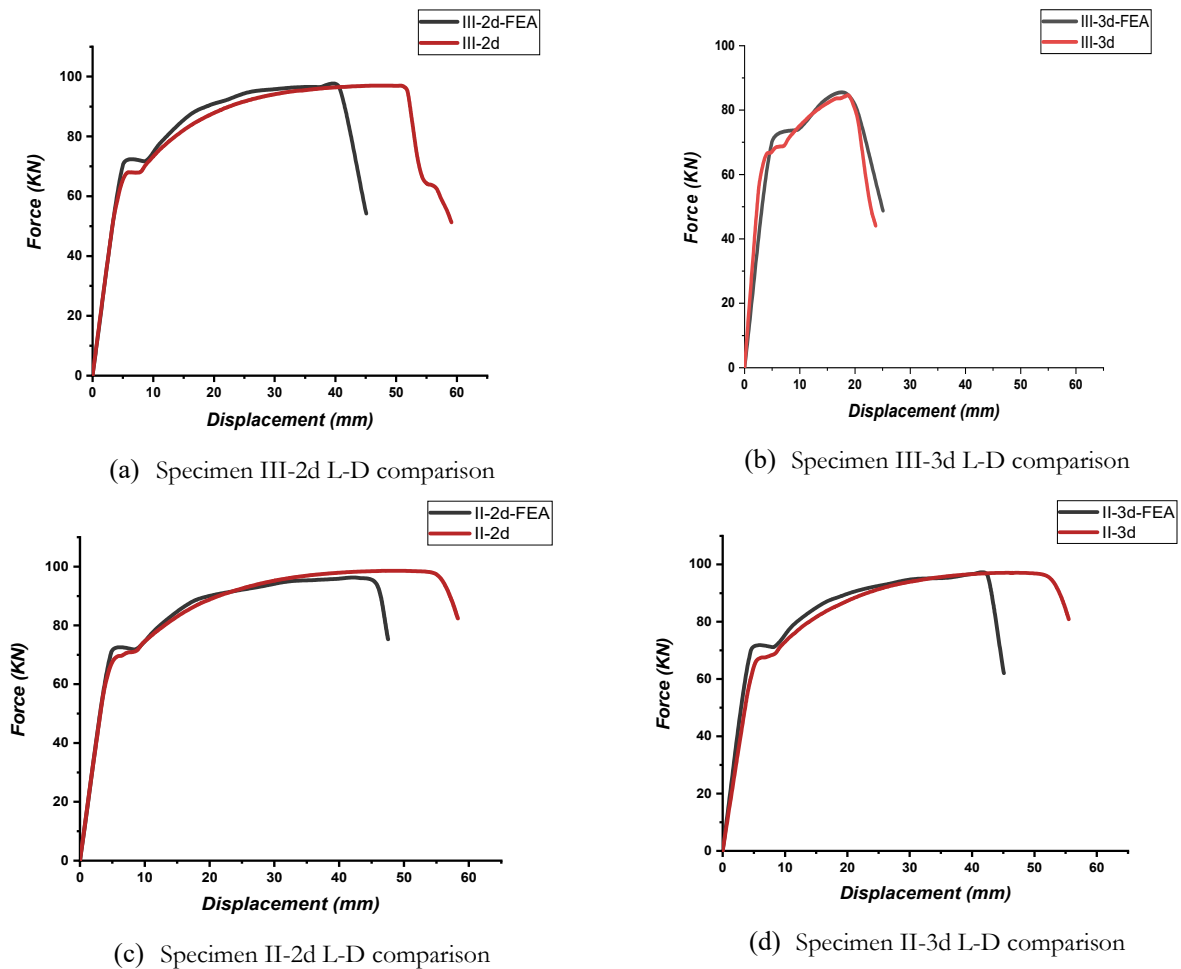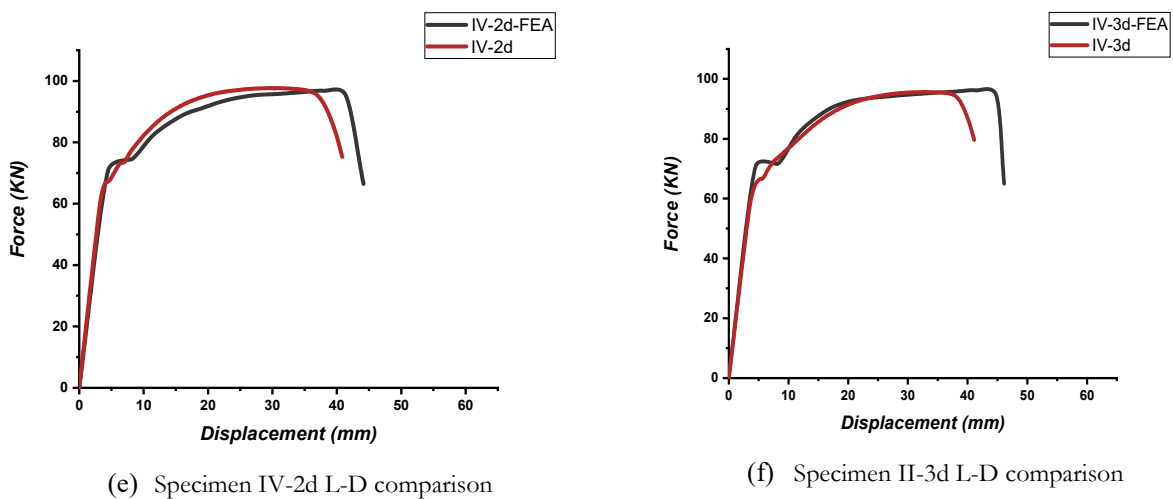
Figure 12: Validation of load-displacement curves

The comparative analysis of the numerical models (FEA) and experimental load-displacement curves indicates that the finite element modelling results are consistent with the experimental findings. The trend of the plots adheres to a similar pattern with close values of the major points, such as the yield and ultimate values. In Fig. 12, the plots reveal that the proposed numerical models accurately predicted the connection's tensile performance, and the interfacial bond-slip model was sensitive to the size and location of the defect.

Failure modes prediction

The proposed models' output predicted the corresponding failure modes of specimens. The numerical model's output database indicates the material's deformation as a result of loading stresses and excessive displacement, which enables the prediction of the failure mode, as shown in Fig. 13.

(a) Experiment Fracture failure   (b) Experiment bond-slip failure

(c) FEA Fracture failure   (d) FEA bond-slip failure
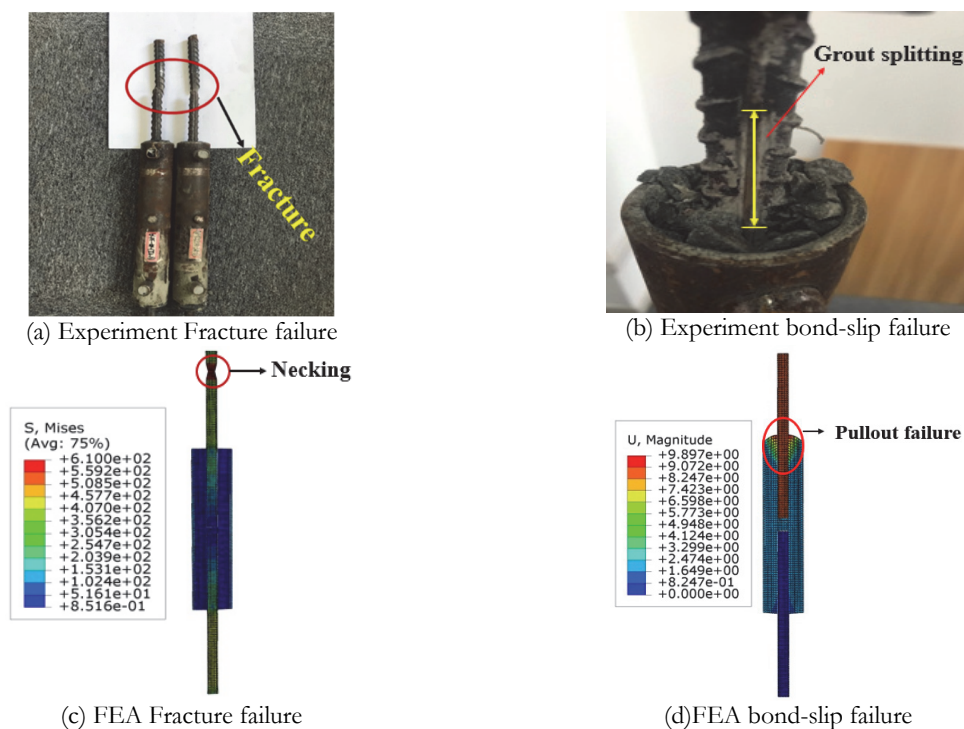
Figure 13: Failure mode prediction

Thus, the experiment has validated the proposed numerical models to conduct accurate simulations of the tensile experiment of the grouted sleeve connections (defective or not). In addition, the influence of defects on the stress distribution within the connection can be analyzed through the computational mechanics of the connection, as shown in Fig. 14.

(i) stress in Grout   (ii) stresses in the Sleeve   (iii) Stresses in the connection

Distribution of stress in a non-defective connection.

(i) Stresses in grout   (ii) Stress in the sleeve   (iii) Stress in Connection

Stress distribution in the defective specimen (III-3d)
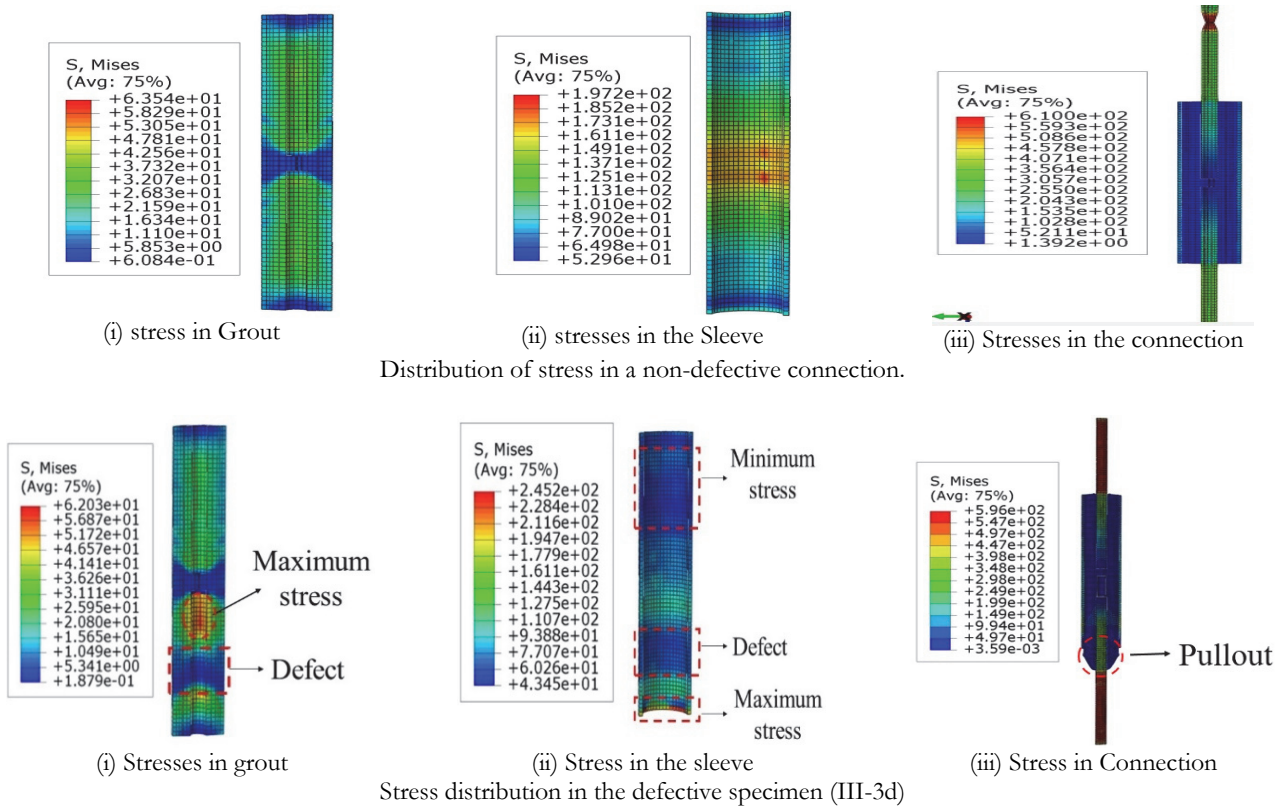
Figure 14: Stress computation of the connection

Tensile stresses are symmetrically and equally distributed between the loading side and the fixed end side of the connection in declining order from the mid-span (clamping zone) of the connection to the edges. Ie. The maximum stress is at the mid-span and decreases toward the edge in the sleeve hall. Whereas in the grouting materials, the clamping zone, which is a "no bonding zone", experienced minor stresses, and the symmetric pattern was observed in grouting materials bonded with the reinforcement while they operate as a medium to transfer resultant stresses from the grout-bar bond to the sleeve. Similarly, the stresses are equally distributed in the reinforcement up to the yielding stage, but in the hardening stage, stresses accumulate in the loading side reinforcement until its fracture. Therefore, a fully grouted sleeve without defects derived its adequate tensile performance from this symmetric and equal distribution of stresses between the loading and fixed end sides.

On the other hand, in Fig. 14 (b), the presence of a defect splits the bonding interface and compromises the influence line and capacity of the bond strength, which enables a transfer of stresses through grouting materials to the sleeve. As a result, stress accumulates in the grouting materials and is transferred heterogeneously rather than symmetrically and equally to the sleeve hall. The accumulation of stress in the grouting materials on the defective side of the connection prompted the pullout failure.

SENSITIVITY ANALYSIS OF THE CONNECTION

Specimens Configurations

The connection's sensitivity analysis is conducted based on the validated numerical models. This analysis aims at identifying the changes in the performance indices of the connection as the defect changes its position. Only the defects of sizes 2d and 3d are considered in this section. The impact of the defect is analyzed at four (4) different locations in the zone of high impact (configuration III), i.e. at a distance (1d), (2d), (3d), and (4d) from the edge of the

connection. For conformity with the experiments in this paper, the defects are predesigned on the lower reinforcement, as shown in Fig. 15.

Furthermore, this analysis considers the confinement effect by the ratio of the diameter of the sleeve to that of the bar d_s/d to assess its influence on the performance indices of the defective specimens. The required design value of the ratio d_s/d for good confinement ranges between (2.66-3.55) [57]. The experiment herein assessed the influence of the confinement effect by considering the ratio's value at 2.66, 3.2 and 3.55. The corresponding specimen labels are S for the lower limit of the interval (2.66), N for the medium value (3.2) corresponding to the diameters' ratio in the above experiment, and L for the upper limit of the interval (3.66). Therefore specimens are labelled in the order III-L-3d-(1d) where III is the configuration, L is the ratio, 3d is the defect's size and (1d) is the defect's location from the edge.
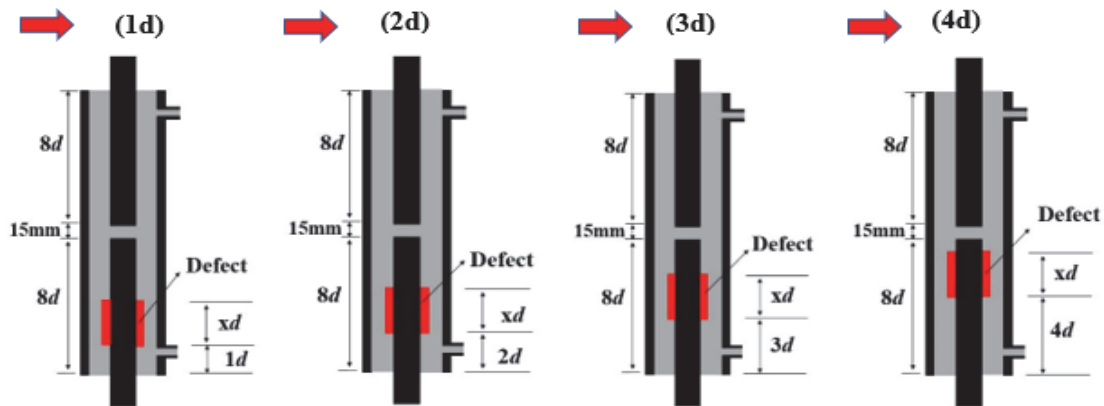
Figure 15: Defects configuration for sensitivity analysis

Location-based impact of grouting defects

In order to provide accurate and relevant technical information to the construction industry, the performance indices of the connection were analyzed based on the geometrical configurations of the commercial sleeve, the confinement effect, and the defects' location at each 1d distance along the anchorage length of the bar, as shown in Fig. 16. As discussed below, the detection of the defect's location should be rationally linked to its adequate risk assessment on the connection's performance. The connection's performance changed drastically as the defect changed the location along the anchorage length, especially when the defect's size was 3d (42mm). Obviously, specimens with defects of size 3d (42mm) had lower bearing capacity than those with defect's size 2d (28mm). The plots indicate that the connection's ultimate capacity decreased gradually as the defect's location shifted away from the edge of the connection up to the distance (3d). Thus the highest drop in the connection's bearing capacity is experienced when the defect's location is at a distance (3d) away from the edge. Beyond this location, at a distance (4d), the connection's ultimate capacity improves as the defect approaches the mid-span, where the defect has a mild impact, as shown in Fig. 17.

On the other hand, the different degrees of confinement influences the connection's tensile performance. The trend observed in the performance of the connection is that defective specimens with the lowest value of the d_s/d ratio have a better performance due to the "small" thickness of grouting materials which enables efficient transfer of resultant stresses to the iron sleeve. As the thickness of the grouting material enlarges, the performance of the connection declines. This phenomenon results from weakened confinement pressure that compromises the grout-bar bond performance. Recently, Hosseini et al. [58] had similar findings and observed a 14% improvement of the bond strength as a result of spiral confinement during the pullout test on precast concrete beams connected with grouted sleeve connection. Nonetheless, the numerical specimens showed a similar pattern in their susceptibility to the location of the defects even when the degree of confinement changed, yet, the latter influenced the bearing capacity of defective specimens, as shown in Fig. 17.

The findings plotted in Fig. 17 demonstrate that the impact of the defect on the connection's load-bearing capacity changed at each (1d) distance from the edge. In addition, the difference in confinement substantially influenced the connection's performance within the prescribed design interval of the d_s/d ratio, i.e. when the design value of the ratio changed from the lowest value, III-S-3d-(3d) to the upper limit, III-B-3d-(3d), the difference in the bearing capacity was 17kN, as noticed in Fig. 17. Furthermore, under the combined impact of the defect's location and confinement effect, the ultimate bearing capacity of the connection was 56kN in the specimen III-L-3d-(3d) below the design load (68kN - 71kN). Out of 12 specimens inbuilt with defects of size 3d, 4 specimens had their load-bearing capacity approximate to the design value

(yielding stage) and below, indicating a serious threat to the connection's structural integrity. Such values are encircled in red in Fig. 17.

(a) Specimen S-2d

(b) Specimen S-3d

(c) Specimen M-2d

(d) Specimen M-3d

(e) Specimen L-2d

(f) Specimen L-3d
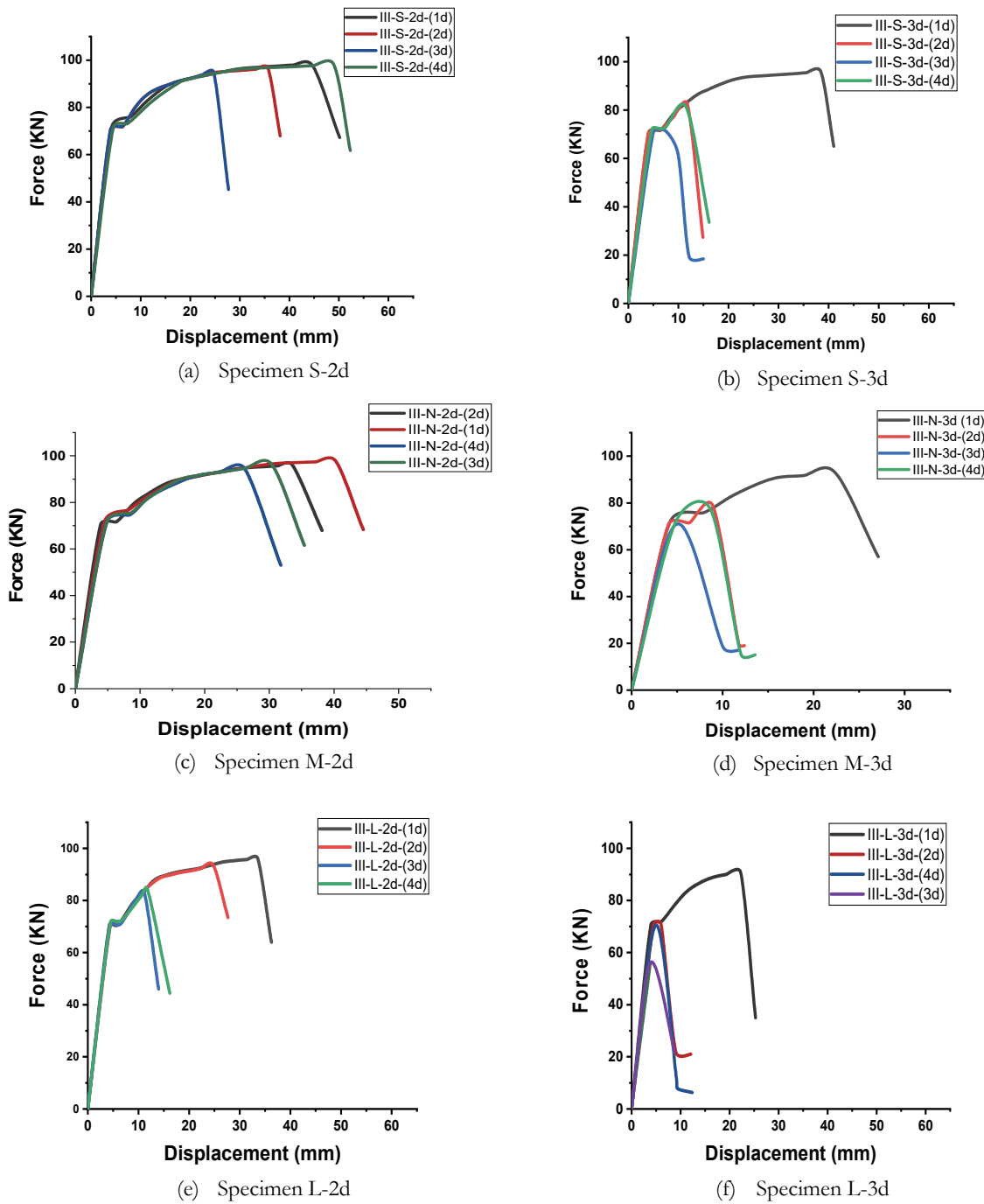
Figure 16: Sensitivity analysis through load-displacement curves

Therefore, a size-based characterization and analysis of grouting defects in the connection are insufficient to enlighten an accurate diagnosis and risk assessment of their impact on the connection's performance. Claims that the bond design value of the connection could be compromised when the defect's size is greater than 3d are valid in one case where the defect is concentrated and located on the edge of the connection. The inclusion of parameters such as the confinement effects and location of defects in the present study has led to contradicting results.

While isolating the reinforcement and the sleeve and making a section (cut) through the 3D simulated specimens, the computational mechanics of stresses on the grout-bar bond interface enables a theoretical diagnosis of the impact of the defects; an example is shown in Fig. 18.

(a) Ratio index S   (b) Ratio index N   (c) Ratio index L
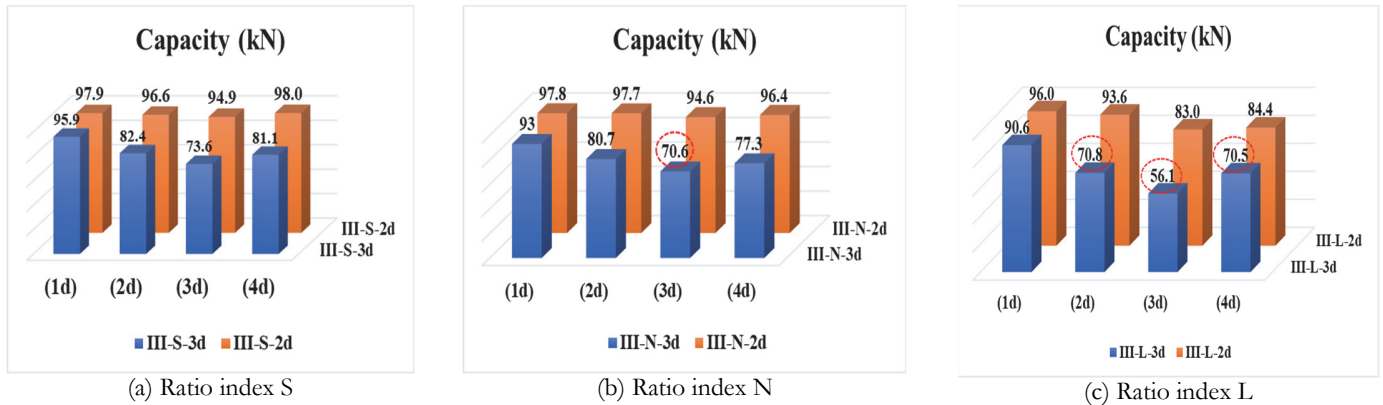
Figure 17: Load bearing capacity of the connection with different configurations

(a) III-S-2d-(3d)   (b) III-N-2d-(3d)   (c) III-L-2d-(3d)

(d) III-S-3d-(3d)   (e) III-N-3d-(3d)   (f) III-L-3d-(3d)
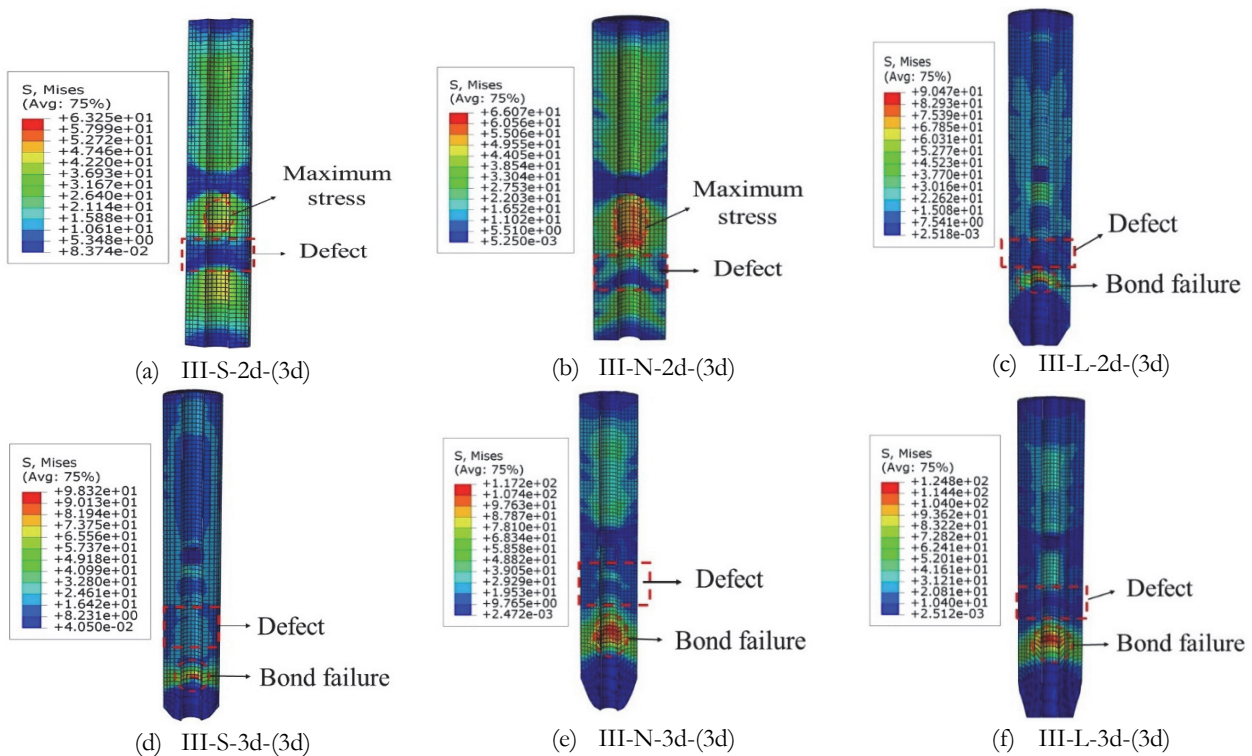
Figure 18: Computation of stresses on the grout-bar interface

Under the impact of the same defect's location and size, the distribution of the resultant stresses on the bonding interface of grouting materials varied based on d_s/d ratio. The deformation of grouting materials during the pullout failure can as well be noticed. As the d_s/d ratio increased, the stresses in the grouting material increased (at the bonding interface). The defect creates clusters of This phenomenon further explains the higher bearing capacity of the specimens with the lower value of the ratio. Therefore, except for major constraints in actual construction, a small thickness of grouting materials while maintaining adequate clearance is a rational choice for an improved mechanical response of the connection and cost-effectiveness (sparing grouting materials).

Deriving a series of equations relating grouting defects to their impact on the connection would be a tedious process and requires a wide range of assumptions since the impact of defects on the connection's performance is non-homogeneous

and is influenced by geometric and mechanical configurations of the connection. Nevertheless, this work proposes a safety constant to improve the accuracy of the calculation of the bond strength when the anchorage length is ≤ 6d. The proposed equation is:

$$\mu' = f_c' \frac{P}{\pi d_b l_e}$$

(4)

μ' is the bond strength, P is the ultimate applied load, d is the diameter of the bar and l_e is the effective anchorage length ≤ 6d and f_c' is the constant of safety accounting for the confinement pressure and the defect in the proposed equation.

The safety constant can change values based on the degree of confinement in the ultimate state design for the bond strength $f_c' = 0.92$ when the d_s/d ratio index is S {2.66-3.0}, $f_c' = 0.67$ when the d_s/d ratio index is N {3.0-3.2} and $f_c' = 0.56$ when the d_s/d ratio index is l {3.2-3.55}.

In addition, a monitoring and maintenance model is proposed based on the findings of this study to enlighten the diagnosis and maintenance of the defective connection in the construction industry.

Proposed diagnosis and maintenance model
Based on the study on the location-based influence of grouting defects in this research, the proposed structural monitoring model of the grouted sleeve connection can be successfully implemented. In addition to the mechanical and geometrical characteristics of the connection, the detection of the defect's location through NDTs would be sufficient to guide a reliable risk assessment of the defects on the grouted sleeve connection. The proposed model relies on a combined analysis of geometric parameters of the connection, the confinement effect, the location and size of the defect to suggest the required action, as shown in Fig. 19.

The above model can be easily implemented in actual construction and computerized to save and replicate relevant geometric and mechanical parameters of the connection and the defect's location and size to enhance efficient structural monitoring and maintenance during and after construction. The proposed model is supported by a risk assessment catalogue proposed in Tab. 9.
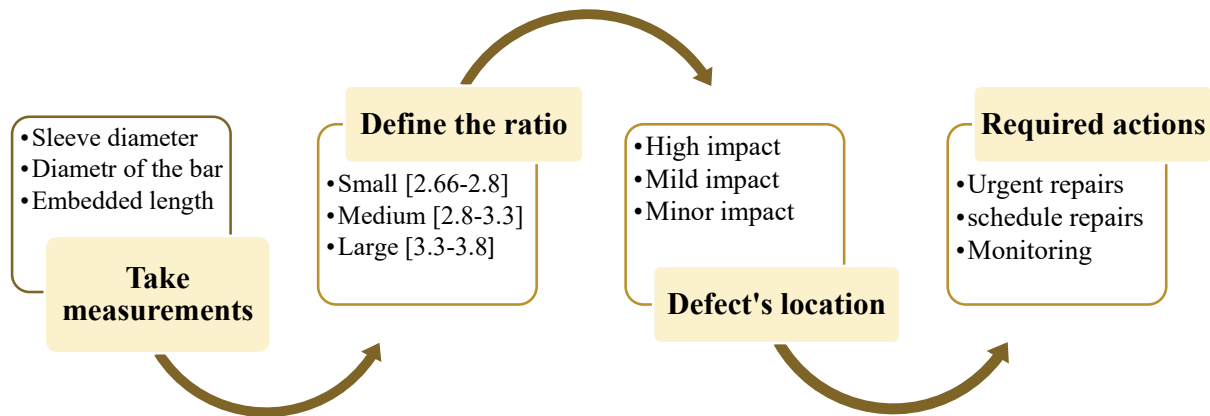
Figure 1: Defects diagnosis model and required actions.

The above catalogue summarizes the risks and impact of defects on the connection's performance to suggest the required maintenance action based on a case by case analysis.

d_s/d ratio index value	Configuration / Defect's location	Risk assessment		Impact on the failure mode		Required action
		Defect 3d	Defect 2d	Defect 3d	Defect 2d	
	III	High	High	Drop 12%	Slip-out	Urgent repair
S {2.66-2.8}	II	Minimum	Minimum	-	-	Repair
	IV	Minimum	Minimum	-	-	Monitoring
	III	High	High	Drop 19.6%	Slip out	Urgent repair
N {2.8-3.3}	II	Mild	Minimum	Slip out	-	Repair
	IV	Minimum	Minimum	-	-	Monitoring
	III	High	High	Drop 44%	Drop 15%	Urgent repair
L {3.3-3.55}	II	High	Mild	Drop 8%	Slip out	Urgent repair
	IV	Mild	Mild	Slip out	Slip out	Repair

Table 9: Risk assessment catalogue.

CONCLUSIONS

This paper presents an assessment of the impact of grouting defects based on their location on the performance of the grouted sleeve connection by analyzing 22 specimens with 7 configurations of defects subjected to a uniaxial tensile experiment. A finite element model which accurately predicts the tensile capacity of the defective grouted sleeve connection is proposed, validated and used to conduct numerical simulation-based sensitivity analysis of the grouted sleeve connection to the location of the defects. Based on the analysis results, the following conclusions were drawn:

✓ The connection's bearing capacity dropped by 19.6% when the defect (size 3d) split the effective bonding length (5d) into two. In contrast, the connection with a continuous bond of 5d anchorage length with the defect of size 3d on edge experienced a drop between 0% - 5% in its bearing capacity and failed by fracture. The connection's response to the defect's location was divided into minor, mild, and high-impact locations.

✓ The connection's bearing capacity considerably changes based on the location of the defect at every distance 1d (14mm) along the grout-bar bonding interface. The drop in capacity decreases as the defect shifts position away from the edge up the distance (3d), beyond which the capacity slightly increases as the defect approaches the mild impact location of the defect.

✓ When the total anchorage length is 8d, the widespread claim that the grout-bar bond strength could be compromised only when the defect's size is greater than 3d undermines the impact of the defect's location and of the confinement effects, which, when included as in this study, have led to contradicting results. This claim, however, is only valid when the defect is concentrated on the edge of the connection.

✓ A location-based assessment of grouting defects' impact on the performance of the full grouted sleeve connection is a promising step toward establishing an efficient parameters-based diagnosis model and risk assessment of the defective connection and appropriate planning of the maintenance action. A diagnosis model and a risk assessment catalogue are proposed in this work.

✓ Different degrees of confinement in the design value interval of the ratio of the sleeve's diameter to that of the bar (ds/d) significantly impact the connection's performance. When the defect of size 3d is located in the mid-span anchorage length, and the ds/d ratio is 2.66, the drop in the ultimate capacity is 19%. In the same location, when ds/d is 3.55, the drop in capacity is 44% below the design requirement. Thus, except for practical constraints, maintaining the ratio at a lower value can optimize the connection's performance.

✓ The connection had better performance when the same defect was replicated on both the upper and lower reinforcements bond interfaces than when located on only one end. This phenomenon indicated that the connection responded positively to the equilibrium in the bearing capacity between the two bonding interfaces.

ACKNOWLEDGMENT

DECLARATIONS

Conflict of Interests: The authors declare that they have no conflict of interest.
Data availability: All experimental data and numerical simulations data and files used to complete this work can be made available by the corresponding author upon reasonable request.

REFERENCES

[1] Ghayeb, H.H., Razak, H.A., and Sulong, N.R. (2020). Performance of dowel beam-to-column connections for precast concrete systems under seismic loads: A review. Construction and Building Materials 237, pp. 117582. DOI: 10.1016/j.conbuildmat.2019.117582.

[2] Alias, A., Zubir, M.A., Shahid, K.A., and RAhman, A.B.A. (2013). Structural performance of grouted sleeve connectors with and without transverse reinforcement for precast concrete structure. Procedia Engineering 53, pp. 116-123. DOI:10.1016/j.proeng.2013.02.017.

[3] Xiao, J., Liu, L., Ding, T., and Xie, Q. (2020). Experimental study on the mechanical behaviour of thermally damaged grouted sleeve splice under cyclic loading. Structural Concrete 21(6), pp. 2494-2514. DOI: 10.1002/suco.202000092.

[4] Kriz, L.B. and Raths, C.H. (1965). Connections in precast concrete structures: strength of corbels. PCI Proceedings paper.

[5] Yang, C., Zhang, L., Zhang, Z., Cao, X., Khan, I., Deng, K., and Xu, T. (2020). Effective stress-strain relationship for grouted sleeve connection: Modeling and experimental verification. Engineering Structures 210, pp. 110300. DOI: 10.1016/j.engstruct.2020.110300.

[6] Sayadi, A.A., Rahman, A.B.A., Jumaat, M.Z.B., Alengaram, U.J., and Ahmad, S. (2014). The relationship between interlocking mechanism and bond strength in elastic and inelastic segment of splice sleeve. Construction and Building Materials 55, pp. 227-237. DOI: 10.1016/j.conbuildmat.2014.01.020.

[7] Zhao, C., Zhang, Z., Wang, J., and Wang, B. (2019). Numerical and theoretical analysis on the mechanical properties of improved CP-GFRP splice sleeve. Thin-Walled Structures 137, pp. 487-501. DOI: 10.1016/j.tws.2019.01.018.

[8] Wang, J., Zhou, J., Pan, M., and Zhang, D. (2016). Experimental study on Bond slip relationship of Steel sleeve. MATEC Web of Conferences, EDP Sciences.

[9] Yuan, H., Zhenggeng, Z., Naito, C.J., and Weijian, Y. (2017). Tensile behavior of half grouted sleeve connections: Experimental study and analytical modeling. Construction and Building Materials 152, pp. 96-104. DOI: 10.1016/j.conbuildmat.2017.06.154.

[10] Lu, Z., Huang, J., Li, Y., Dai, S., Peng, Z., Liu, X., and Zhang, M. (2019). Mechanical behaviour of grouted sleeve splice under uniaxial tensile loading. Engineering Structures 186, pp. 421-435. DOI: 10.1016/j.engstruct.2019.02.033.

[11] Espoir, K.K., Fuzhe, X., and Haojie, G. (2020). Grouted Sleeve Connection for Precast Concrete Members. Civil Engineering Journal 28 (4), pp.435-447. DOI: 10.14311/CEJ.2020.04.0038.

[12] Ling, J.H., Rahman, A.B.A., Ibrahim, I.S., and Hamid, Z.A. (2012). Behaviour of grouted pipe splice under incremental tensile load. Construction and Building Materials 33, pp. 90-98. DOI: 10.1016/j.conbuildmat.2012.02.001.

[13] Ling, J.H., Rahman, A.B.A., and Ibrahim, I.S. (2014). Feasibility study of grouted splice connector under tensile load. Construction and Building Materials 50, pp. 530-539. DOI: 10.1016/j.conbuildmat.2013.10.010.

[14] Lin, F. and Wu, X. (2016). Mechanical performance and stress-strain relationships for grouted splices under tensile and cyclic loadings. International Journal of Concrete Structures and Materials 10(4), pp. 435-450. DOI 10.1007/s40069-016-0156-5.

[15] Jiang, T., Wu, Z., Huang, L., and Ye, H. (2020). Three-dimensional nonlinear finite element modeling for bond performance of ribbed steel bars in concrete under lateral tensions. International Journal of Civil Engineering, pp. 1-23. DOI: 10.1007/s40999-019-00488-1.

[16] Hosseini, S.J.A. and Rahman, A.B.A. (2015). Effects of spiral diameter on the bond stressslip relationship in grouted sleeve connector. Malaysian Constr Res J (MCRJ) 12(1).

[17] Singhal, S., Chourasia, A., and Kajale, Y. (2021). Cyclic behaviour of precast reinforced concrete beam-columns connected with headed bars. Journal of Building Engineering 42, pp. 103078. DOI: 10.1016/j.jobe.2021.103078.

[18] Murakami, R., Onoue, K., Morimoto, K., and Hashimoto, R. (2021). Effects of expansive filler and headed rebar on the shortening of development length of mortar-filled joints. Journal of Building Engineering 40, pp. 102338. DOI: 10.1016/j.jobe.2021.102338.

[19] Gao, Q. and Zhao, W. (2021). Experimental study on factors influencing the connection performance of grouted welded sleeves under uniaxial tensile loads. Journal of Building Engineering 43, pp. 103033. DOI:10.1016/j.jobe.2021.103033.

[20] Haber, Z.B., Saiidi, M.S., and Sanders, D.H. (2014). Seismic performance of precast columns with mechanically spliced column-footing connections. ACI Structural Journal 111(3), pp. 639-650. DOI: S-2012-286.R2.

[21] Tullini, N. and Minghini, F. (2016). Grouted sleeve connections used in precast reinforced concrete construction–Experimental investigation of a column-to-column joint. Engineering Structures 127, pp. 784-803. DOI: 10.1016/j.engstruct.2016.09.021.

[22] Ameli, M. and Pantelides, C.P. (2017). Seismic analysis of precast concrete bridge columns connected with grouted splice sleeve connectors. Journal of Structural Engineering 143(2), pp. 04016176. DOI: 10.1061/(ASCE)ST.1943-541X.0001678.

[23] Ameli, M., Brown, D.N., Parks, J.E., and Pantelides, C.P. (2016). Seismic column-to-footing connections using grouted splice sleeves. ACI Structural Journal 113(5), pp. 1021. DOI: 10.14359/51688755.

[24] Qu, H., Li, T., Wang, Z., Wei, H., Shen, J., and Wang, H. (2018). Investigation and verification on seismic behavior of precast concrete frame piers used in real bridge structures: Experimental and numerical study. Engineering Structures 154, pp. 1-9. DOI:10.1016/j.engstruct.2017.10.069.

[25] Tong, C., Wu, J., Li, C., Han, J., and Li, Z. (2021). Experimental investigation of a single-yielding precast concrete beam–column connection with replaceable energy-dissipation connector. Soil Dynamics and Earthquake Engineering 150, pp. 106906. DOI: 10.1016/j.soildyn.2021.106906.

[26] Tong, C., Wu, J., and Li, C. (2021). A novel precast concrete beam-to-column connection with replaceable energy-dissipation connector: experimental investigation and theoretical analysis. Bulletin of Earthquake Engineering 19(12), pp. 4911-4943.DOI: 10.1007/s10518-021-01144-7.

[27] Desmettre, C., Charron, J.-P., and Gendron, F. (2021). Design and Performance of a Precast Bridge Barrier with Ultra-high Performance Fibre Reinforced Concrete (UHPFRC). in RILEM-fib International Symposium on Fibre Reinforced Concrete, Springer. DOI: 10.1007/978-3-030-83719-8_41.

[28] DeJong, A., Shi, W., Shafei, B., and Hosteng, T. (2021). Integral Abutment Connections with Grouted Reinforcing Bar Couplers and Ultrahigh-Performance Concrete. Journal of Bridge Engineering 26(8), pp. 04021042. DOI: 10.1061/28ASCE29BE.1943-5592.0001732.

[29] Wang, Z., Zhu, J., Wang, J., Zhao, G., Sun, S., and Zhang, J. (2021). Experimental study on a novel UHPC grout-filled pipe sleeve with mechanical interlocking for large-diameter deformed bars. Engineering Structures 226, pp. 111358. DOI: 10.1016/j.engstruct.2020.111358.

[30] Li, X., Xiao, S., Gao, R., Harries, K.A., Wang, Z., and Xu, Q. (2021). Effects of grout sleeve defects and their repair on the seismic performance of precast concrete frame structures. Engineering Structures 242, pp. 112619. DOI: 10.1016/j.engstruct.2021.112619.

[31] Xiao, S., Wang, Z., Li, X., Harries, K.A., Xu, Q., and Gao, R. (2021). Study of effects of sleeve grouting defects on the seismic performance of precast concrete shear walls. Engineering Structures 236, pp. 111833. DOI: 10.1016/j.engstruct.2020.111833.

[32] Guo, T., Yang, J., Wang, W., and Li, C. (2022). Experimental investigation on connection performance of fully-grouted sleeve connectors with various grouting defects. Construction and Building Materials 327, pp. 126981. DOI: 10.1016/j.conbuildmat.2022.126981.

[33] Kahama, E.K., Fuzhe, X., and M. Anglaaere, D.-L. (2021). Numerical study on the influence of defects in grouting on the mechanical properties of a full grouted sleeve connector. The Journal of Adhesion, pp. 1-32. DOI: 10.1080/00218464.2021.1982389.

[34] Xu, F., Wang, K., Wang, S., Li, W., Liu, W., and Du, D. (2018). Experimental bond behavior of deformed rebars in half-grouted sleeve connections with insufficient grouting defect. Construction and Building Materials 185, pp. 264-274. DOI: 10.1016/j.conbuildmat.2018.07.050.

[35] Zheng, G., Kuang, Z., Xiao, J., and Pan, Z. (2020). Mechanical performance for defective and repaired grouted sleeve connections under uniaxial and cyclic loadings. Construction and Building Materials 233, pp. 117233.

DOI: 10.1016/j.conbuildmat.2019.117233.

[36] Zhang, W., Wang, J., Zhang, J., Cao, Y., Qin, P., and Yi, W. (2020). Experimental study on post-fire performance of half grouted sleeve connection with construction defect. Construction and Building Materials 244, pp. 118165. DOI: 10.1016/j.conbuildmat.2020.118165.

[37] Chen, J., Wang, Z., Liu, Z., and Ju, S. Experimental investigation of mechanical behaviour of rebar in steel half-grouted sleeve connections with defects in water/binder ratio. in Structures. 2020. Elsevier. DOI: 10.1016/j.istruc.2020.04.051.

[38] Raza, A., ur Rehman, A., Masood, B., and Hussain, I. Finite element modelling and theoretical predictions of FRP-reinforced concrete columns confined with various FRP-tubes. in Structures. 2020. DOI: 10.1016/j.istruc.2020.04.033..

[39] Gu, S., Wu, Y., Wang, X., Li, S., Ding, C., and Wu, Y. (2020). Nondestructive testing of strength of sleeve grouting material in prefabricated structure based on surface hardness method. Construction and Building Materials 263, pp. 120675. DOI: 10.1016/j.conbuildmat.2020.120675.

[40] Zhou, Z., Wu, H., Tan, C., Xing, Y., and Gao, R., (2021). Comparison and a case study of test methods for sleeve grouting fullness in precast bridge piers, in Life-Cycle Civil Engineering: Innovation, Theory and Practice. CRC Press, pp. 971-976.

[41] Xu, B., Fan, X., Wang, H., Zhou, S., Wang, C., Chen, H., and Ge, H. (2021). Experimental study on grout defects detection for grouted splice sleeve connectors using stress wave measurement. Construction and Building Materials 274, pp. 121755. DOI: 10.1016/j.conbuildmat.2020.121755.

[42] Liu, H., Qi, Y., Chen, Z., Tong, H., Liu, C., and Zhuang, M. (2021). Ultrasonic inspection of grouted splice sleeves in precast concrete structures using elastic reverse time migration method. Mechanical Systems and Signal Processing 148, pp. 107152. DOI: 10.1016/j.ymssp.2020.107152.

[43] Li, Z., Zheng, L., Chen, C., Long, Z., and Wang, Y. (2019). Ultrasonic detection method for grouted defects in grouted splice sleeve connector based on wavelet pack energy. Sensors 19(7), pp. 1642. DOI: 10.3390/s19071642.

[44] Parks, J.E., Papulak, T., and Pantelides, C.P. (2016). Acoustic emission monitoring of grouted splice sleeve connectors and reinforced precast concrete bridge assemblies. Construction and Building Materials 122, pp. 537-547. DOI: 10.1016/j.conbuildmat.2016.06.076.

[45] Feng, K., Zhao, Q., and Qiu, Y. (2020). Damage imaging in mesoscale concrete modeling based on the ultrasonic time-reversal technique. Acta Mechanica Solida Sinica 33(1), pp. 61-70. DOI: 10.1007/s10338-019-00153-z.

[46] Zhang, X., Zhou, D., Tang, H., and Han, X. (2019). Experimental study of grout defect identification in precast column based on wavelet packet analysis. International Journal of Distributed Sensor Networks 15(11). DOI: 1550147719889590.

[47] Tang, H., Xie, Y., Zhao, T., and Xue, S. (2020). Identification of grout sleeve joint defect in prefabricated structures using deep learning. Frontiers in Materials, pp. 298. DOI: 10.3389/fmats.2020.00298.

[48] Lubliner, J., Oliver, J., Oller, S., and Onate, E. (1989). A plastic-damage model for concrete. International Journal of solids and structures 25(3), pp. 299-326. DOI: 10.1016/0020-7683(89)90050-4.

[49] Malm, R. (2006). Shear cracks in concrete structures subjected to in-plane stresses. KTH, School of Architecture and the Built Environment (ABE), Civil and Architectural Engineering, Structural Design and Bridges.

[50] Hany, N.F., Hantouche, E.G., and Harajli, M.H. (2016). Finite element modeling of FRP-confined concrete using modified concrete damaged plasticity. Engineering Structures 125, pp. 1-14. DOI: 10.1016/j.engstruct.2016.06.047.

[51] Kmiecik, P. and Kamiński, M. (2011). Modelling of reinforced concrete structures and composite structures with concrete strength degradation taken into consideration. Archives of civil and mechanical engineering 11(3), pp. 623-636. DOI: 10.1016/S1644-9665(12)60105-8.

[52] Szczecina, M. and Winnicki, A. (2016). Selected aspects of computer modeling of reinforced concrete structures. Archives of Civil Engineering 62(1). DOI: 10.1515/ace-2015-0051.

[53] Cervenka, V., Cervenka, J., and Kadlec, L. (2018). Model uncertainties in numerical simulations of reinforced concrete structures. Structural Concrete 19(6), pp. 2004-2016. DOI: 10.1002/suco.201700287

[54] Dere, Y. and Koroglu, M.A. (2017). Nonlinear FE modeling of reinforced concrete. International Journal of Structural and Civil Engineering Research 6(1), pp. 71-74. DOI: 10.18178/ijscer.6.1.71-74.

[55] Ma, Y.-X., Zhao, O., and Tan, K.H. (2021). Experimental and numerical studies of concrete-encased concrete-filled steel tube stub columns under uniaxial and biaxial eccentric compression. Engineering Structures 232, pp. 111796. DOI: 10.1016/j.engstruct.2020.111796.

[56] Ren, W., Sneed, L.H., Yang, Y., and He, R. (2015). Numerical simulation of prestressed precast concrete bridge deck panels using damage plasticity model. International Journal of Concrete Structures and Materials 9(1), pp. 45-54. DOI: 10.1007/s40069-014-0091-2.

[57] Brenes, F.J., Wood, S.L., and Kreger, M.E. (2006). Anchorage requirements for grouted vertical-duct connectors in precast bent cap systems. Center for Transportation Research The University of Texas at Austin.

[58] Hosseini, S.J.A., Rahman, A.B.A., Hwang, H.-J., Hosseini, S.K., and Kang, S.-M. (2022). Bond behaviour of spirally confined bar splices in the grout. Construction and Building Materials 327, pp. 127060. DOI: 10.1016/j.conbuildmat.2022.127060.